JOURNAL OF SPACECRAFT AND ROCKETS
Vol. 32, No. 6, November–December 1995

Flow Through a Submerged Nozzle

Brian E. Thompson,* Olivier Bouchery,† and K. D. Lowney‡
Rensselaer Polytechnic Institute, Troy, New York 12180-3590

Measurements of mean and fluctuating velocity components are obtained with refractive-index-matching laser velocimetry in a submerged nozzle representative of thrust-vectoring nozzles in solid rocket motors. The approaching flow has a structure similar to that approaching a sudden contraction, but is affected by the large annular recirculation bubble that fills the outer annular cavity around the nozzle and reattaches on the nozzle lip. Turbulence production is increased, with large fluctuations in the shear layer bounding the recirculation bubble and core flow. Immediately upstream of the nozzle; this production is balanced by relaminarization processes associated with acceleration of core flow into the nozzle. The development of the wall flow inside the nozzle is significantly different from that in a simple nozzle, and the present measurements provide benchmark data that give insight into turbulence modeling assumptions used in procedures to design solid rocket motors.

Nomenclature

D	= diameter of the upstream duct, mm
d	= diameter of the nozzle at the throat, mm
n	= refractive index
R	= local radius from the centerline to the wall, mm
Re	= Reynolds number
r	= radial position (origin on the centerline), mm
T	= temperature, K
U, V	= mean components of axial and radial velocity, m/s
u, v	= fluctuating components of axial and radial velocity, m/s
x	= axial position (origin in the plane of the nozzle tip), mm
ν	= dynamic viscosity, m^2/s
ρ	= density, kg/m^3

Subscripts

b	= bulk
d	= downstream duct
u	= upstream duct

Introduction

SOLID rocket motors (SRMs) are rocket engines in which the propellant, composed of fuel and oxidizer, is stored in solid form upstream of a nozzle. The burning characteristics, which determine the thrust, mass flow rate, operating pressure, and burn duration of an SRM, depend on the size and shape of the exposed burning surface: inhibitors are often located in and around the grain to control overall burn rate of the rocket.

Two nozzle configurations are commonly used in modern solid rocket boosters: an external, convergent–divergent nozzle, or a submerged nozzle similar to that shown in Fig. 1. Submerged nozzles have the entry, the throat, and part of the exit duct cantilevered upstream into the combustion chamber to allow for thrust vectoring mechanisms. Design of submerged nozzles is more complex than that of external nozzles because the former are exposed to hotter gases, particulate, and external pressure forces.[1] Submergence lowers specific impulse by about 1%, mostly on account of the first 10–15% of submergence.[2] Submerged nozzles are, however, preferred in many solid rocket motors because of their thrust-vectoring capability.

Chunks of inhibitor or solid propellant released from the grain surface react while convecting through the SRM nozzle. Experiments[3] in combination with calculations of gas–particle flowfields[3,4] suggest these particles can affect rocket performance in several ways. Metal oxide particles can cause momentum losses because of their velocity lag and failure to transfer chemical energy to the gases.[5] Combustion efficiency can be affected by the size distribution of released aluminum oxide particles.[6] Convecting metal oxide particles can influence boundary-layer development and separation bubbles, and can lead to heat, pressure, and recombination losses.[5] Calculations of two-phase flow in solid rocket motors[6,7] affirm that particulate influences momentum transfer and thus the size and location of the annular recirculation region on the submerged exterior of the nozzle entrance, and thus exacerbates the overall SRM performance loss associated with submergence.

The flowfield inside models of solid rocket motors with submerged nozzles has been calculated,[6–9] and results compared with experiments in models of SRM geometries.[1,10,11] Confidence in the calculations is, however, limited because of uncertainties associated with boundary-condition and numerical approximations and assumptions in models of turbulence, heat transfer, and multiphase flow. Quantitative data from experimental investigations are essential for comparison to calculations and for validation of modeling assumptions, and are the subject of the present work.

Experimental investigations inside combusting solid rocket motors are difficult. Measured results for computational fluid dynamics (CFD) validation purposes have been mainly obtained in water models and cold-gas simulations of flow through SRM configurations. Water models are used because they have low cost and show separated-flow regions.[1] Schorr,[12] Hoyt,[13] Adams,[14] and many

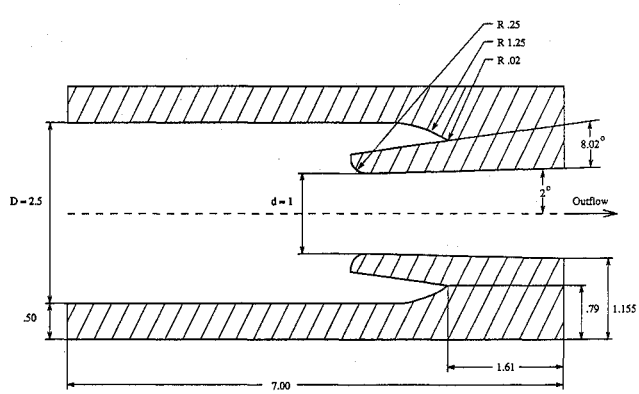

Fig. 1 Geometry of axisymmetric submerged nozzle. (Dimensions are shown in inches.)

Received Nov. 28, 1994; revision received April 27, 1995; accepted for publication April 28, 1995. Copyright © 1995 by the authors. Published by the American Institute of Aeronautics and Astronautics, Inc., with permission.

*Associate Professor, Department of Mechanical Engineering, Aeronautical Engineering and Mechanics. Member AIAA.

†Graduate Student, Department of Mechanical Engineering, Aeronautical Engineering and Mechanics.

‡Graduate Student, Department of Mechanical Engineering, Aeronautical Engineering and Mechanics; currently affiliated with the U.S. Air Force.

studies at NASA Marshall Space Flight Center used water models to study the complex flow patterns in SRM nozzle geometries. Cold-air flow models have also simulated flow through SRM nozzles[2,15,16] and measured the exhaust flow to obtain viscous-flow properties, turbulence characteristics, heating rates, and erosion patterns. Visualization of flow patterns at a burn time of 100 s in an $\frac{1}{8}$-scale model of the Space Shuttle SRM, with nozzle vectoring capability and wall injection, showed that vortex formation upstream of the nozzle inlet influenced exhaust patterns.[10] Hot-wire measurements obtained in injection-driven cavities with geometric similarity to SRMs show that the axial velocity near the nozzle is not constant near the centerline and gradients increase substantially near the walls in response to turbulent shear.[11] The effect of particles in the flow was not obtained, because the porous wall made it difficult to arrange sensible particle injection and an appropriate measurement system: for example, fragile hot wires would be immediately damaged in this fluid–particle mixture, and optical diagnostics was impractical through porous (hence opaque) walls. It is also difficult to extend these techniques to multiphase experiments, because of problems in scaling particle size and distribution. Accordingly, emphasis was placed here on measurement of single-phase flow for validation of the fluid-transport models before adding complexities such as wall blowing, heat transfer, and combusting particles.

Investigations of erosive burning in solid rocket motors[17,18] have measured the burn-time variation. Variations in propellant mass, propellant density, and characteristic velocity were small enough to have nearly negligible effects on burn-time dispersion in most solid rocket motor designs.[17] A fixed geometry of an SRM flowfield at a given burn time is used here.

The complex geometry, especially near the submerged nozzle entrance, makes access difficult for optical diagnostics. Laser Doppler velocimetry (LDV) obtains the flow velocity nonintrusively, but its application would be limited around the multiple solid boundaries and curved surfaces of a submerged nozzle. Optical distortion associated with differences in the refractive indices between the model material and the fluid along the path of the laser beams would affect the measurement position and frequency–velocity conversion of the LDV, or may prevent measurement because the beams do not intersect to form an interference volume.

Refractive-index-matching laser velocimetry (RIMLV) alleviates the above optical-access difficulties by matching the refractive indices of the model and fluid. Several RIMLV techniques have been used,[19–22] each with its own advantages and limitations. Glass models[20,21] are costly and difficult to manufacture, and associated fluids that match the refractive index of glass often have high viscosities, which make obtaining high-Reynolds-number flows also costly and difficult. The present investigation chose instead a low-viscosity mixture of organic solvents that matches to acrylic.[19,22] Thompson[23] reported this solution was used in acrylic models to obtain velocity measurements and visualization in flow through a variety of complex models, including a Space Shuttle main engine (SSME) preburner liquid-oxygen post, a scaled model of the SSME main injector bowl,[19] a scaled model of a rotating SSME bearing cavity, a centrifugal pump,[22] a coal combustor, an engine intake manifold, and dense two-phase flows.[24] This RIMLV approach was chosen for the present submerged nozzle because it avoids flow interference associated with probes, it is not frustrated with the optical accessibility limitations, and it can attain high Reynolds numbers in the turbulent regime at reasonable cost. It can also be extended to two-phase flows.

The present model, flow system, and measurement procedures are described next and followed by measured results including flow visualization, mean velocity, and turbulence quantities. The development of the mean flow and the structure of the turbulence approaching and inside the nozzle, which includes the balancing processes between turbulence production and relaminarization, are then discussed, and the paper closes with the salient conclusions.

Apparatus and Procedure

Model of the Submerged Nozzle

Figure 1 shows the 1.8%-scale geometry of the present acrylic model, which has an axisymmetric core of submerged nozzle at a 100-s burn time in the Space Shuttle SRM. Dimensions were based on those measured in solid rocket motor nozzles[10] and are similar to those of models in previous studies.[6–8,10,11,25] The inlet and exhaust regions of the present model are long pipes, which makes computational grid generation and calculations straightforward, keeps model manufacturing at a reasonable cost, and is a simplification of SRM configurations. The acrylic model has flat exterior walls to simplify optical access and allow measurements of axial and radial components of velocity throughout the flow. To alleviate residual stresses that could effect optical clarity and model life, the acrylic block was first annealed at 420 K for 12 h, which resulted in about 2% shrinkage. The block was then rough machined to within about 0.05 mm of its final dimensions, and annealed for a second time at 410 K for 11 h. The model was then machined and polished to the dimensions shown in Fig. 1.

Refractive-Index-Matching Flow Circuit

Figure 2 shows the refractive-index-matching circuit, which comprises a temperature-controlled reservoir, a pump, a flowmeter, and the model described above. The refractive index of the fluid and acrylic were matched so that the optical path of the laser light was unaffected and determination of the position and geometric characteristics of the measurement volume inside the model was straightforward. A mixture of turpentine and Tetralin was held at a constant temperature to match refractive indices, and Table 1 presents its properties.

Table 2 presents the present operating conditions. The flow rate was obtained with a rotameter. The most important parameters to match in this flow are the geometry and the Reynolds number at the nozzle throat. Geometric scaling was discussed above. Table 3 presents a comparison of actual and model operating parameters, which show that the Reynolds number in the refractive-

Table 1 Properties of the refractive-index-matched mixture

Density	$\rho = 900$ kg/m^3
Kinematic viscosity at 32°C	$\nu = 1.54 \times 10^{-6}$ m^2/s
Refractive index	$n = 1.489$
Temperature	$T = 32$°C

Table 2 Operating conditions

Volume flow rate	20 gal/min
Bulk mean velocity at nozzle throat	2.80 m/s
Bulk mean velocity upstream duct	0.5 m/s
Matching temperature	32°C

Table 3 Similarity parameters

Parameter	Actual SRM	Model
Nozzle throat Reynolds number	2×10^6	4.6×10^4
Nozzle throat diameter d, m	1.4	0.254
Upstream duct diameter D, m	3	1.61
D/d	2.1	2.5

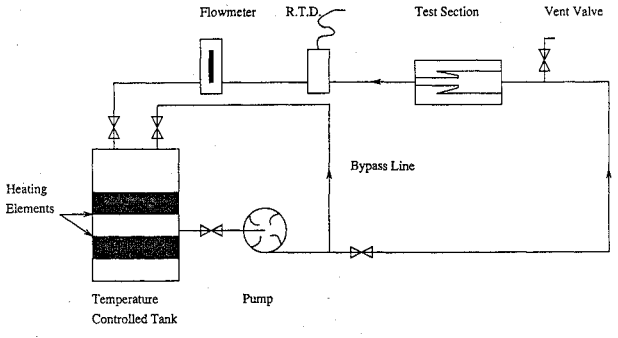

Fig. 2 Refractive-index-matching flow circuit.

index-matching flow circuit is sufficiently high to obtain turbulent flow in the invariant range between 10^4 to 10^7 for SRM geometries.[10]

Flow Visualization

Flow visualization was obtained with conventional photographic techniques, including a high-intensity light, camera, and video recorder. Small air bubbles were created in the fluid to scatter the light for photography. These bubbles were created by mixing air with the fluid mixture in the temperature-controlling tank and then using the pump to break any large bubbles into an almost uniform distribution of about 0.5-mm-diam bubbles. The quantity of bubbles was controllable, although their size was not.

Laser Velocimeter

The laser velocimeter comprised a 15-mW He–Ne laser (632.8-nm wavelength), backscatter transmitting and receiving optics, a three-axis traversing mechanism, a cascade photodiode, a counter with signal conditioner, and a microcomputer. Optics were configured for a measurement volume with length and diameter of 2.1 and 0.13 mm, respectively. Flow was seeded with acrylic spheres of 2-μm diameter. The counter was arranged in 10–16 frequency validation mode after setting appropriate amplitude validation levels with a digital oscilloscope. The optical setup did not include a frequency-shifting device: flow visualization identified regions with reversing flow, which were not measured here.

Measurement Uncertainty

Maximum uncertainties for 95% confidence in the mean velocities and turbulence intensities reported below were less than 2 and 6% of the local values based on the optical characteristics of the RIM flow circuit and signal-processing instrumentation, and these were repeatable within 1%. The mean flow rate was monitored within 1%, and the RIMLV measurement volume was positioned within 0.02 mm with a tridirectional, linear traversing mechanism.

Measured Results

Flow Visualization

Figure 3 shows the overall flow pattern obtained from flow visualization. Turbulent, fully developed, axisymmetric, swirl-free flow (as confirmed by measurements below) approaches the nozzle entrance. The most prominent flow feature is the annular recirculation bubble around the nozzle exterior. In turbulent boundary layers like those found in this flow configuration, separation does not occur at a single streamwise location, but is spread over a streamwise region and involves a spectrum of states.[26,27] The onset of separation is indicated by the appearance of reverse flow, and fully developed separation is achieved when the mean wall shear stress vanishes. For the present configuration and flow rate, the location of mean streamline detachment was at 0.44d upstream of the nozzle entrance, and the mean-flow reattachment point was on the tip of the nozzle nose.

Velocity Measurements

Measurements of axial and radial components of velocity are presented upstream and downstream of the submerged nozzle entrance, although not in the recirculating flow region previously discussed. Figure 4 gives the axial components of mean velocity and turbulence intensity along the centerline of the nozzle. The mean flow

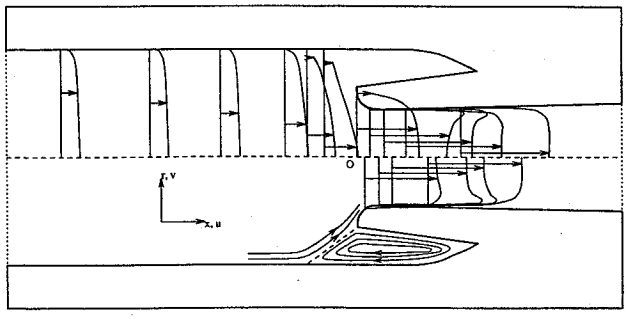

Fig. 3 Flow structure and axial mean velocity in the submerged nozzle.

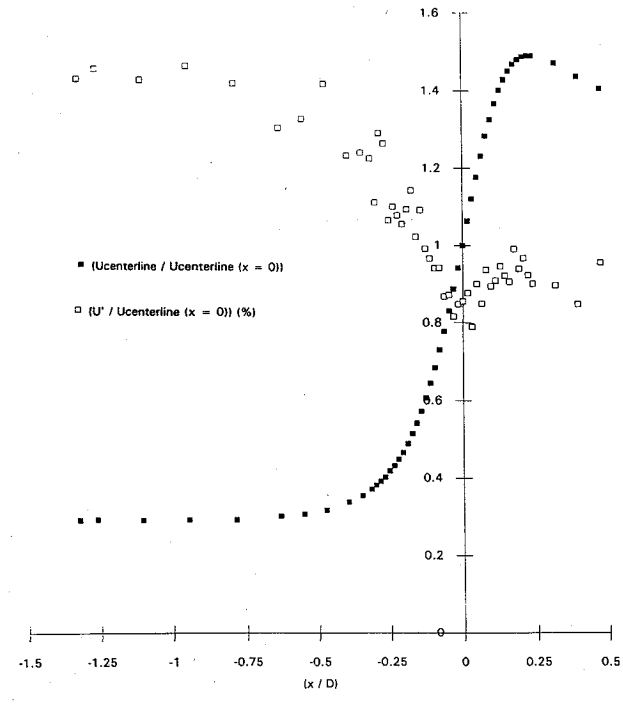

Fig. 4 Axial components of mean velocity and turbulence intensity along the centerline.

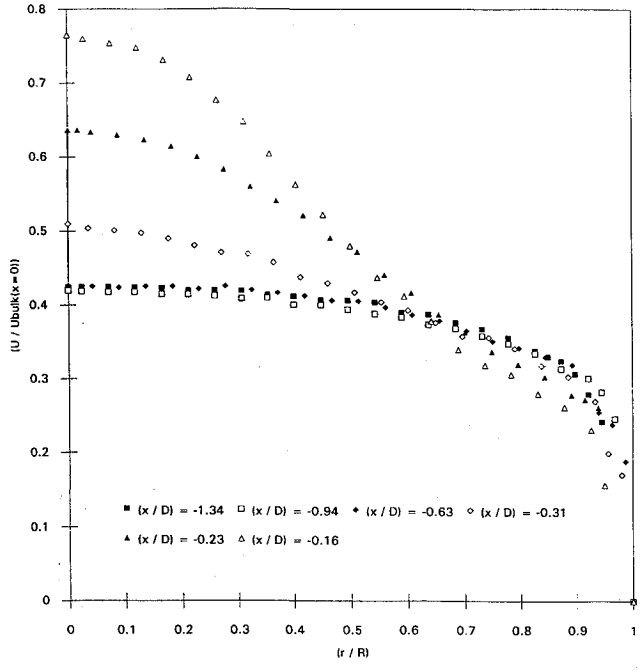

Fig. 5 Axial component of mean velocity upstream of the nozzle entrance.

accelerates, gradually approaching the nozzle, until it reaches its maximum value at the nozzle throat. Downstream of the throat, the core expands at a 2-deg angle, which causes deceleration of the core flow leaving the nozzle. Turbulence intensity in the upstream flow is low and is further reduced by relaminarization processes associated with mean-flow acceleration approaching the nozzle.

Figures 5 and 6 present measured values of axial and radial components of the mean velocity, respectively, which were obtained upstream of the nozzle entrance. At the inlet 1.4D upstream of the nozzle entrance, the flow is axisymmetric, fully developed, turbulent pipe flow; this is a result of the combination of plenum, flow straighteners, and screens located about 30D further upstream. Approaching the nozzle entrance, the mean component of axial velocity accelerates near the centerline and decelerates near the wall as the

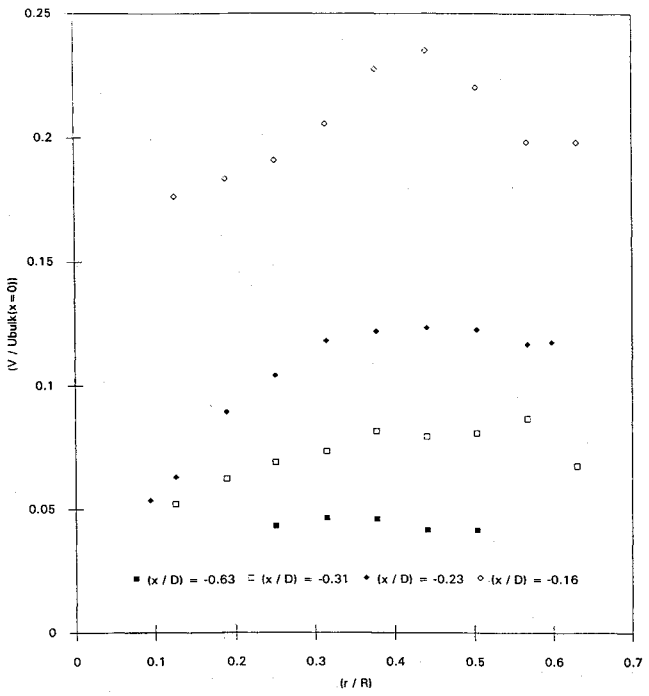

Fig. 6 Radial component of mean velocity upstream of the nozzle entrance.

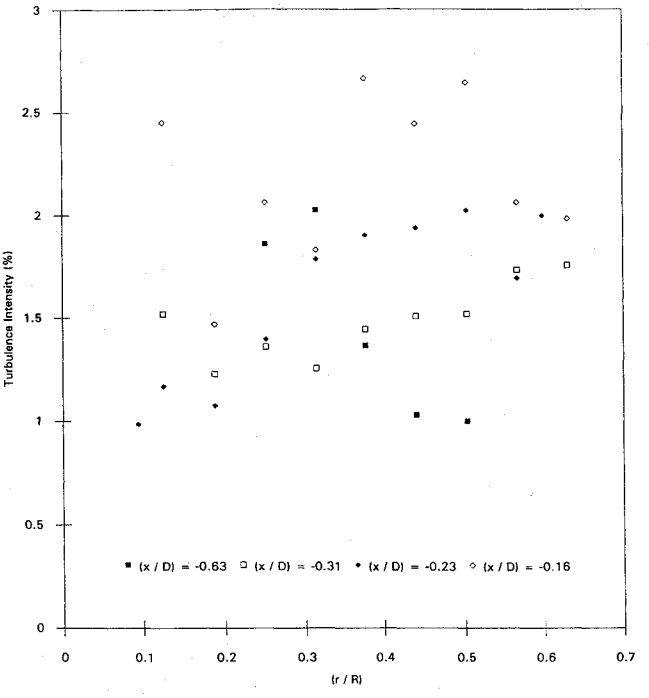

Fig. 8 Radial component of turbulence intensity upstream of the nozzle entrance.

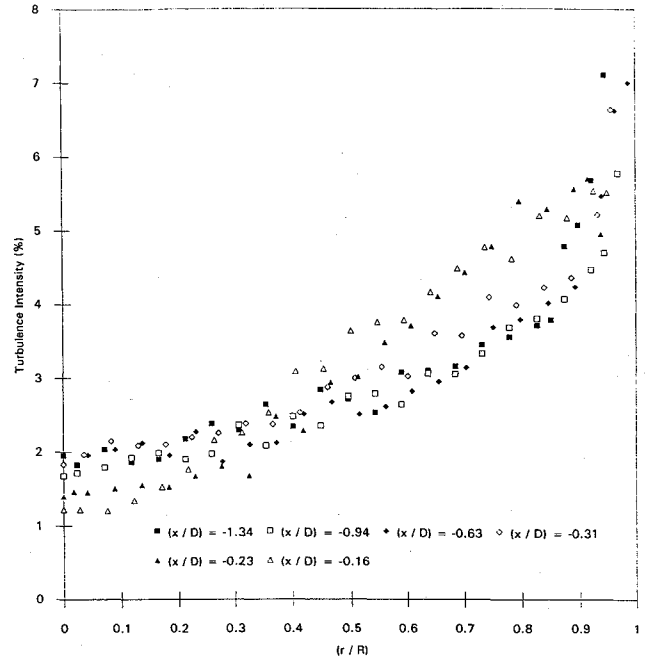

Fig. 7 Axial component of turbulence intensity upstream of the nozzle entrance.

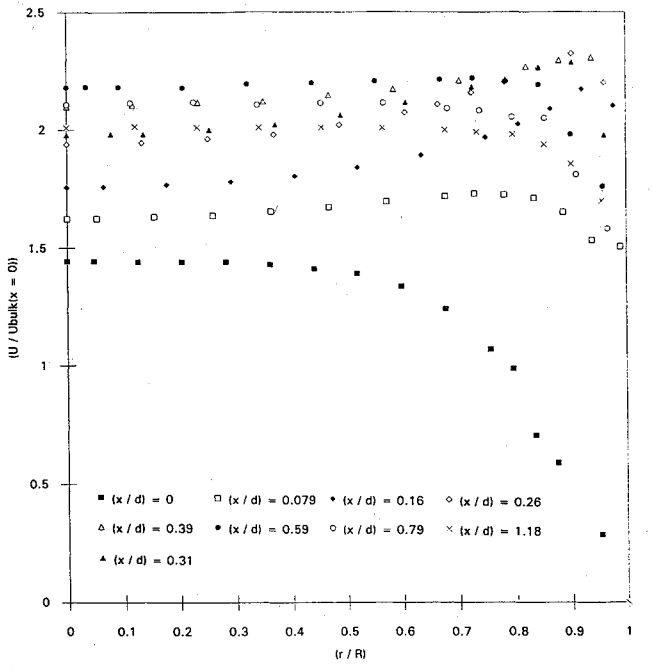

Fig. 9 Axial component of mean velocity downstream of the nozzle entrance.

flow adjusts to enter the nozzle. The radial component of mean velocity exceeds 5% of the bulk velocity at about $x/D = -0.6$ upstream of the nozzle entrance, although the redistribution of axial velocity is small. At about $0.25D$ upstream of the nozzle, the axial component of velocity has lost its pipe-flow distribution and has characteristics more typical of flow upstream of a forward-facing step. The radial velocity has its largest value of about 25% of bulk velocity at about $0.15D$ upstream of the nozzle, where the near-wall flow has separated as discussed below. The two profiles within x/D of -0.25 of the entrance have regions near the wall where the flow is reversing and measurement uncertainty is high.

Figures 7 and 8 show measurements of axial and radial components of turbulence intensity, respectively, at locations corresponding to the above mean-flow results. Axial turbulence intensity has a typical pipe-flow distribution that has been affected by two influences. First, turbulence production in the annular shear layer that separates the recirculating flow and accelerating core flow increases velocity fluctuations at x/D between about -0.8 and -0.4. Second, the near-wall flow is approaching separation, and the maximum turbulence intensity decreases and moves away from the wall: these characteristics are typical of wall flow approaching separation.[27] The largest measured values of radial normal stresses were found at the center of the shear layer at about $0.15D$ upstream of the nozzle, which corresponds with the location of both the maximum gradient of the axial velocity and the largest values of the radial velocity, both of which were found at r/R about 0.5.

An annulus of recirculating flow is observed around the external surface of the nozzle. The mean streamline detachment was located by flow visualization at about $0.6d$ upstream of the nozzle entrance

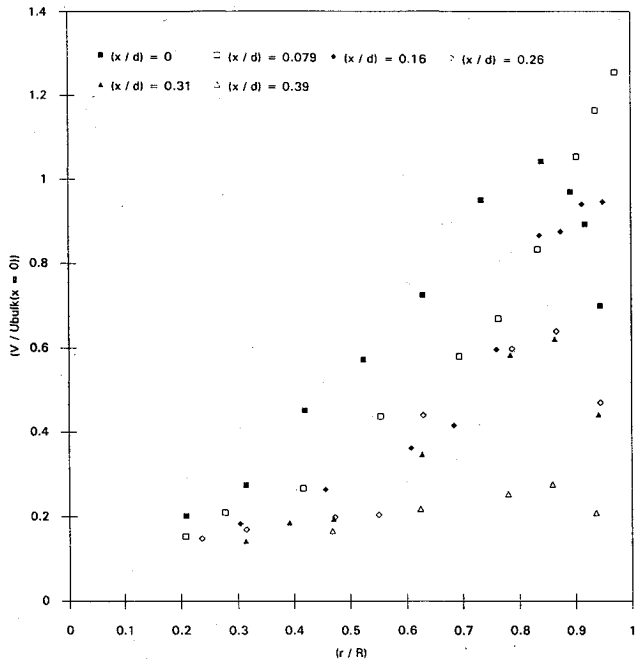

Fig. 10 Radial component of mean velocity downstream of the nozzle entrance.

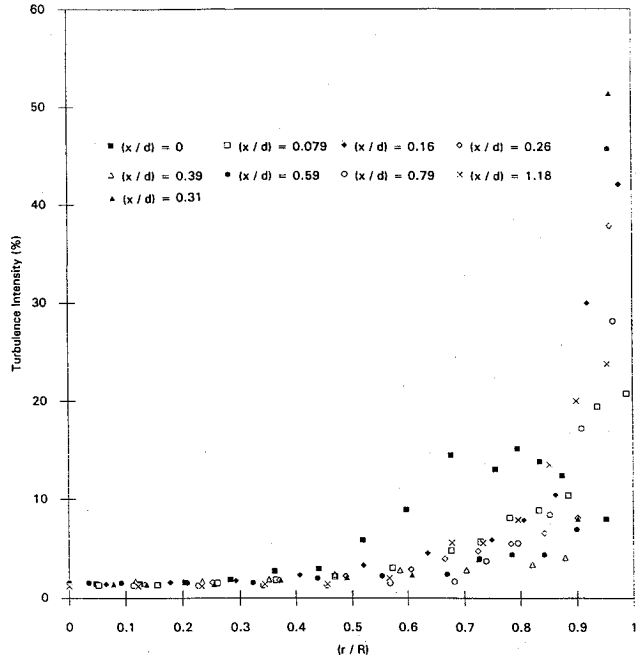

Fig. 11 Axial component of turbulence intensity downstream of the nozzle entrance.

on the outer wall. Reattachment was apparent on the upstream tip of the nozzle in flow visualization.

Figures 9 and 10 show measured values of axial and radial components of mean velocity inside the nozzle. Flow entering the nozzle at $x/d = 0.0$ has a distorted axial profile. The radial components of velocity near the nozzle tip are larger than the axial components as the flow turns around the tip and enters the nozzle. The axial velocity develops a peak near the wall at about $x/d = 0.16$, which increases to a maximum value at x/d about 0.39 and then recovers towards a pipe-flow distribution downstream. Correspondingly, the radial component of the mean velocity is significant but decreasing from the tip to about $x/d = 0.39$, where it becomes small and dominated by the 2-deg expansion of the duct. Figures 11 and 12 show the corresponding axial and radial turbulence intensities. Turbulence levels in the wall boundary layers are affected by the mean-flow acceleration, which effects relaminarization between $x/d = 0.0$ and 0.08.

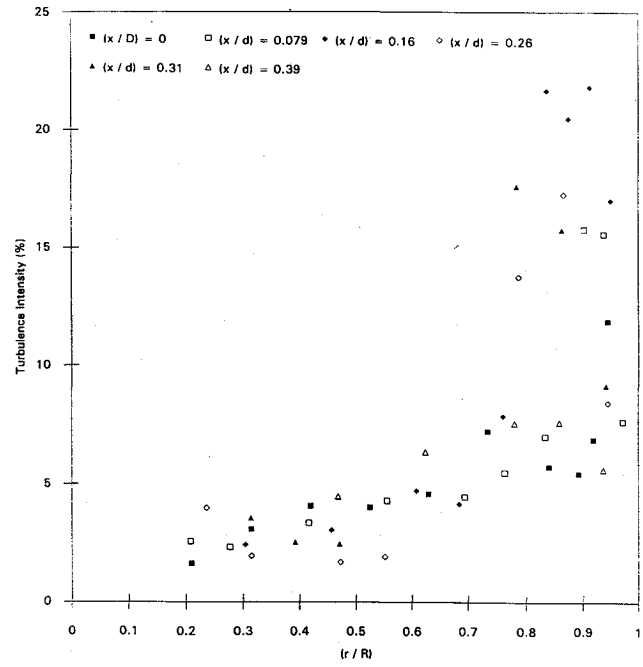

Fig. 12 Radial component of turbulence intensity downstream of the nozzle entrance.

Downstream of this location, turbulence production near the wall dominates over relaminarization, and turbulence levels increase, although at a lower rate than would be expected in developing flow regions in straight or diffusing ducts. The mean flow and turbulence have developed characteristics typical of conventional pipe flow within $1.18d$ downstream of the nozzle tip.

Discussion

The present flow represents a simplification of the multiphase flow, heat transfer, phase change, and chemical reactions found in solid rocket motors. The present configuration is of interest because it assesses the influence of the complex geometry of the submerged nozzle on flow development, without the complicating effects of wall blowing, particle size and distribution, and compressibility. If simpler cases like this or, for example, flow through sudden contractions can be shown to be valid comparisons for certain characteristics of the flowfield inside the actual nozzle, then numerical and experimental investigations based on them may provide a means for obtaining insights into significant phenomena and for validating calculation procedures.

Measurements of flows in a pipe with a sudden contraction have been reported for contraction ratios D/d and Reynolds numbers based on the upstream duct diameter of 1.87 and 1000 in the laminar regime,[28] and of 1.6 and 10,000 in the turbulent regime,[29] and can be compared with 2.5 and 20,000 for the submerged-nozzle results presented above. The bulk flow accelerates as it enters these nozzles, and this dominates the flow patterns of all three configurations. These patterns are also similar to previous calculated[9] and measured[10] results obtained in various configurations representative of SRM geometries. This acceleration also causes turbulence fluctuations in the core flow to decrease with increasing downstream distance along the duct centerline. Measurements in the present submerged nozzle, measurements in the turbulent sudden-contraction flow,[29] and also calculations in complex nozzle flows with mixing length and k–ε turbulence models[8] confirm this relaminarization effect.

In both of these laminar and turbulent sudden-contraction flows, an outer annular recirculation region is observed in the corner upstream of the contraction. Another annular separation bubble is observed downstream of the sharp edge at its entrance. While the former is observed in the present results and in other experiments in SRM nozzle flows,[10] the latter is not observed here, because the flow reattaches at the lip and then remains attached to the curved surface from there downstream into the small duct.

Distributions of mean velocity in both turbulent and laminar flows approaching the sudden contraction have similarities to those measured in the present submerged nozzle. The flow near the centerline increases in velocity because of streamline convergence, and the velocity gradients near the wall decrease and approach separation. Downstream of the nozzle entrance, a maximum of mean axial velocity is measured near the wall. This feature is also found in calculated and measured results in the laminar sudden-contraction flow,[28] although the maximum values are smaller with the smaller contraction ratio. This near-wall acceleration is not reported in the turbulent flow through a sudden contraction,[29] perhaps because velocity measurements could not be obtained until almost 1 diameter downstream of the contraction step without the use of refractive-index-matching laser velocimetry.

In laminar sudden-contraction flows, both length and height of the recirculation region upstream of the contraction depend on Reynolds number.[28] The distance from the small-duct entrance upstream to the location of mean-flow detachment on the outer wall is at most about half that in the present submerged-nozzle flow. The laminar reattachment point is not found at the sharp edge of the entrance to the small duct, but is always more than 20% of the step height outward from the sharp edge towards the outer wall at the contraction. In the submerged nozzle, reattachment is found at the lip of the nozzle nose.

The details of flow development in the vicinity of the submerged nozzle are different from both laminar and turbulent flows through sudden contractions. The submerged-nozzle flow has less curvature in shear layer surrounding the recirculation bubble, and there is more gradual development of the boundary layer on the nozzle surface downstream of the lip.

Discontinuities at the contraction step are absent in the present geometry and the surface of the tip of the present model curves gradually as its diameter contracts to that of the exit duct. The influence of streamwise curvature[30] is expected to be negligible, the ratio of boundary-layer thickness to surface radius being less than 0.3. The swirl component of the mean velocity was negligible, so there was no evidence of secondary streamwise vortices or their effects on the turbulence structure as observed with large streamwise curvature.[31] Laminarization processes[32] are dominant in this region of the nozzle entrance.

The influence of wall blowing is negligible[7] in the immediate vicinity of a submerged nozzle in an SRM at late burn times. As the grain surface recedes with burn time, solid surfaces are exposed in the vicinity of the nozzle and its outer annular chamber. The annular recirculating flow interacts with the core flow in the conical shear layer that accelerates the core flow into the nozzle inlet. Flow on the outer wall and downstream of this shear layer recirculates inside the outer annular cavity by traveling along the boundary towards the centerline and continuing around the cavity wall back towards the separation point. The present flowfield is similar to that measured in gas flow through a model of a Space Shuttle SRM with wall blowing.[10] Both show separated flow in the cavity region and acceleration of core flow as it passes through the nozzle inlet.

Concluding Remarks

Measurements of the radial and axial components of the mean and fluctuating velocity have been presented in a submerged nozzle with a geometry chosen to represent the Space Shuttle solid rocket motors at long burn times. Flow approaching the nozzle is dominated by acceleration of the core flow and the annular recirculation region on the outer wall, which separates upstream of the nozzle entrance and reattaches on the lip of the nozzle nose. Measured turbulence quantities show evidence of the balance between relaminarization and wall production in the shear layer approaching and inside the submerged nozzle. The present measurements describe flow characteristics that would allow validation of CFD methods that calculate flow through submerged nozzles.

Acknowledgments

The authors are grateful to Dale Andrews and David Bacchus of NASA Marshall Space Flight Center for many discussions about SRM geometries. We are also pleased to thank Alex Ostrogorsky, James Fairweather, Michael Gilhooley, Ralph Nayler, and William Mielke for assistance with the flow circuit, model fabrication, and instrumentation.

References

[1]Ellis, R. S., and Keller, R. B., "Solid Rocket Motor Nozzles," NASA SP-8115, June 1975.

[2]Salmi, R. J., and Pelouch, J. J., "Investigation of a Submerged Nozzle on a 1/14.2-Scale Model of the 260-Inch Solid Rocket," NASA TM-X-1388, May 1967.

[3]Crowe, C. T., "Review: Numerical Models for Dilute Gas-Particle Flows," *Journal of Fluids Engineering*, Vol. 104, Sept. 1982, pp. 194–204.

[4]Carlson, D. J., and Hoglund, R. F., "Particle Drag and Heat Transfer in Rocket Nozzles," *AIAA Journal*, Vol. 2, No. 11, 1964, pp. 1980–1984.

[5]Timnat, Y. M., *Advanced Chemical Rocket Propulsion*, 1st ed., Academic, New York, 1987, pp. 90–110.

[6]Carrier, G., Fendell, F., Brent, D., Kimbrough, C., Loucks, S., Hess, E., and Acosta, P., "Simple Modeling of Particle Trajectories in Solid Rocket Motors," *Journal of Propulsion and Power*, Vol. 7, No. 2, 1991, pp. 185–195.

[7]Madabhushi, R. K., Sabnis, J. S., de Jong, F. J., and Gibeling, H. J., "Calculation of the Two-Phase Aft-Dome Flowfield in Solid Rocket Motors," *Journal of Propulsion and Power*, Vol. 7, No. 2, 1991, pp. 178–184.

[8]Sabnis, J. S., Gibeling, H. J., and McDonald, H., "Navier–Stokes Analysis of Solid Propellant Rocket Motor Internal Flows," *Journal of Propulsion and Power*, Vol. 5, No. 6, 1989, pp. 657–664.

[9]Hwang, C. J., and Chang, G. C., "Numerical Study of Gas–Particle Flow in a Solid Rocket Nozzle," *AIAA Journal*, Vol. 26, No. 6, 1988, pp. 682–689.

[10]Waesche, R. H. W., and Sargent, W. H., "Space Shuttle Solid Rocket Motor Aft-End Internal Flows," *Journal of Propulsion and Power*, Vol. 5, No. 6, 1989, pp. 650–656.

[11]Dunlap, R., Blackner, A. M., Waugh, R. C., Brown, R. S., and Willoughby, P. G., "Internal Flowfield Studies in a Simulated Cylindrical Port Rocket Chamber," *Journal of Propulsion and Power*, Vol. 6, No. 6, 1990, pp. 690–704.

[12]Schorr, C. J., "Pressure Ratio Correction Factor When Utilizing the Hydraulic Analogy," *Journal of Spacecraft and Rockets*, Vol. 5, No. 9, 1968, pp. 1119–1120.

[13]Hoyt, J. W., "The Hydraulic Analogy for Compressible Gas Flow," *Applied Mechanics Review*, Vol. 15, No. 6, 1962, pp. 419–425.

[14]Adams, D. M., "Application of the Hydraulic Analogy to Axisymmetric Nonideal Compressible Gas Systems," *Journal of Spacecraft and Rockets*, Vol. 4, No. 3, 1967, pp. 359–363.

[15]Sola, F. L., "Development of the Explorer Solid Rocket Motor," *Journal of Propulsion and Power*, Vol. 7, No. 4, 1991, pp. 513–517.

[16]Schetz, J. A., Hewitt, P. A., and Thomas, R., "Swirl Combustor Flow-Visualization Studies in a Water Tunnel," *Journal of Spacecraft and Rockets*, Vol. 20, No. 6, 1983, pp. 574–582.

[17]Heister, S. D., and Davis, R. J., "Predicting Burning Time Variations in Solid Rocket Motors," *Journal of Propulsion and Power*, Vol. 8, No. 3, 1992, pp. 564–569.

[18]Foster, W. A., Jr., Sforzini, R. H., and Shackleford, B. W., Jr., "Thrust Imbalance of Space Shuttle Solid Rocket Motors," *Journal of Spacecraft and Rockets*, Vol. 19, No. 6, 1982, pp. 545–549.

[19]Thompson, B. E., Senaldi, J., Vafidis, C., Whitelaw, J. H., and McDonald, H., "Flow in a Model of the Space Shuttle Main Engine Main Injector Bowl," *Journal of Spacecraft and Rockets*, Vol. 29, No. 2, 1992, pp. 247–252.

[20]Park, J. T.,Mannheimer, R. J., Grimley, T. A., and Morrow, T. B., "Pipe Flow Measurements of a Transparent Non-Newtonian Slurry," *Journal of Fluids Engineering*, Vol. 111, Sept. 1989, pp. 331–336.

[21]Longmire, E. K., and Eaton, J. K., "Structure of a Particle-Laden Round Jet," *Journal of Fluid Mechanics*, Vol. 236, 1992, pp. 217–257.

[22]Liu, C. H., Vafidis, C., and Whitelaw, J. H., "Flow Characteristics of a Centrifugal Pump," *ASME Journal of Fluids Engineering*, Vol. 116, June 1994, pp. 303–309.

[23]Thompson, B. E., "Refractive-Index Matching Techniques in Complex Rocket-Engine Flow Configurations," Scientific Research Associates, Inc., Contractor Rept. R89-900072-F, Glastonbury, CT, Jan. 1990.

[24]Nouri, J. M., Whitelaw, J. H., and Yianneskis, M., "Particle Motion and Turbulence in Dense Two-Phase Flows," *International Journal of Multiphase Flow*, Vol. 13, No. 6, pp. 729–739.

[25]Chang, I., "One- and Two-Phase Nozzle Flows," *AIAA Journal*, Vol. 18, No. 12, 1980, pp. 1455–1461.

[26]Simpson, R. L., Chew, Y. -T., and Shivaprasad, B. G., "The Structure of a Turbulent Separating Boundary Layer," *Journal of Fluid Mechanics*, Vol. 113, No. 2, 1981, p. 23.

[27]Thompson, B. E., and Whitelaw, J. H., Characteristics of a Trailing-Edge Flow with Turbulent Boundary-Layer Separation. *Journal of Fluid Mechanics*, Vol. 157, No. 1, 1985, pp. 305–326.

[28]Durst, F., and Loy, T., "Investigations of Laminar Flow in a Pipe with Sudden Contraction of Cross Sectional Area," *Computers and Fluids*, Vol. 13, No. 1, 1985, pp. 15–36.

[29]Khezzar, L., and Whitelaw, J. H., "Flows Through Round Sudden Contractions," *Journal of Mechanical Engineering Science*, Vol. 202, Jan. 1988, pp. 295–300.

[30]Gibson, M. M., Jones, W. P., and Younis, B. A., "Calculation of Turbulent Boundary Layers on Curved Surfaces," *Physics of Fluids*, Vol. 24, 1981, p. 386.

[31]Bradshaw, P., "Effects of Streamwise Curvature on Turbulent Flow," AGARDograph 169, AGARD, 1973.

[32]Jones, W. P., and Launder, B. E., "The Prediction of Laminarization with a Two-Equation Model of Turbulence," *International Journal of Heat and Mass Transfer*, Vol. 15, No. 1, 1972, p. 301.

J. C. Adams
Associate Editor

Teleoperation and Robotics in Space

Steven B. Skaar and Carl F. Ruoff, editors

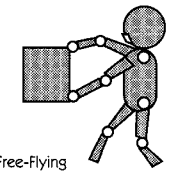

Increasingly, space teleoperators and robots (space telerobots) will take the place of astronauts in planetary and Lunar scientific missions to reduce cost and risk. Terrestrial robots have much in common with space robots, but there are important physical differences arising from weightlessness, vacuum, the thermal environment, and the need to minimize mass. Because the technology for building intelligent space robots does not yet exist, they must be supervised by human operators.

This new book addresses these concerns, providing extensive, well-illustrated descriptions of existing, planned, and laboratory space telerobot systems, international designs, the role and capabilities of humans in system control and supervision, levels of control autonomy, the economic tradeoffs of manned versus telerobotic space operations, and dynamics and control.

Contents (partial):

Introduction
Human-Machine Interface
Human Enhancement and Limitation in Teleoperation
Ground Experiments Toward Space Teleoperation with Time Delay
Toward Advanced Teleoperation in Space
Planning and Perception
Techniques for Collision Prevention, Impact Stability, and Force Control
Versatile and Precise Vision-Based Manipulation
Dynamics and Control
Tutorial Overview of the Dynamics and Control of Satellite-Mounted Robots
Reorientation of Free-Flying Multibody Structure Using Appendage Movement
Transfer Functions of Flexible Beams and Implications of Flexibility on Controller Performance
Telerobot System Design and Applications
Teleoperation: From the Space Shuttle to the Space Station
Overview of International Robot Design for Space Station Freedom
Space Station Robotics Task Validation and Training

Progress in Astronautics and Aeronautics series
1994, 502 pp, illus, Hardback
ISBN 1-56347-095-0
AIAA Members: $79.95 Nonmembers: $99.95
Order #: V-161(945)

Place your order today! Call 1-800/682-AIAA

AIAA
American Institute of Aeronautics and Astronautics
Publications Customer Service, 9 Jay Gould Ct., P.O. Box 753, Waldorf, MD 20604
FAX 301/843-0159 Phone 1-800/682-2422 8 a.m. - 5 p.m. Eastern

Sales Tax: CA residents, 8.25%; DC, 6%. For shipping and handling add $4.75 for 1-4 books (call for rates for higher quantities). Orders under $100.00 must be prepaid. Foreign orders must be prepaid and include a $25.00 postal surcharge. Please allow 4 weeks for delivery. Prices are subject to change without notice. Returns will be accepted within 30 days. Non-U.S. residents are responsible for payment of any taxes required by their government.